Supplementary Information

Symmetrical and Asymmetrical Surface Structure Expansions of Silver Nanoclusters with Atomic Precision

Honglei Shen,[‡a] Pu Wang,[‡b] Jiawei Xu,[a] Ziwei Fu,[a] Xi Kang,*[a] Yong Pei,*[b] and Manzhou Zhu*[a]

[a]Department of Chemistry and Centre for Atomic Engineering of Advanced Materials, Key Laboratory of Structure and Functional Regulation of Hybrid Materials of Ministry of Education, Institutes of Physical Science and Information Technology and Anhui Province Key Laboratory of Chemistry for Inorganic/Organic Hybrid Functionalized Materials, Anhui University, Hefei, Anhui 230601, China.

[b]Department of Chemistry, Key Laboratory of Environmentally Friendly Chemistry and Applications of Ministry of Education, Xiangtan University, Xiangtan, Hunan 411105, P. R. China.

[‡]These authors contributed equally.

*Email: kangxi_chem@ahu.edu.cn (X.K.); ypei2@xtu.edu.cn (Y.P.); zmz@ahu.edu.cn (M.Z.)

This Supplementary Information file includes:

Experimental Methods

Materials

The following reagents were purchased from Sigma-Aldrich and used without further purification: silver nitrate ($AgNO_3$, 99.5% metal basis), 1,3-benzene dithiol (BDT, 98%), triphenylphosphine (PPh_3, 99.0%), sodium borohydride ($NaBH_4$, 99.0%), methylene chloride (CH_2Cl_2, HPLC grade), methanol (CH_3OH, HPLC grade), ethanol (CH_3CH_2OH, HPLC grade), N,N-dimethylformamide (DMF, HPLC grade), and hydrochloric acid (HCl, 0.1 M).

Syntheses

Synthesis of the 3,5-dithiolbenzoic acid (BDTA ligand)

The BDTA ligand was prepared according to the literature method.[1]

Synthesis of the $Ag_{29}(BDT)_{12}(PPh_3)_4$ nanocluster (Ag_{29}-BDT for short)

The $Ag_{29}(BDT)_{12}(PPh_3)_4$ nanocluster was obtained using the literature method.[2]

Synthesis of the $Ag_{29}(BDTA)_{12}(PPh_3)_4$ nanocluster (Ag_{29} for short)

The Ag_{29} nanocluster was synthesized via a one-pot method. Specifically, 40 mg of $AgNO_3$ (0.24 mmol) was dissolved in 5 mL of CH_3OH and 10 mL of DCM. The obtained solution was stirred vigorously (~1500 rpm) for 10 minutes. Then, 20 mg of BDTA (0.16 mmol) and 262 mg of PPh_3 (1 mmol) were added. The reaction was stirred vigorously for another 30 minutes. Then, 1 mL of the $NaBH_4$ aqueous solution (15 mg/mL) was added quickly to the above mixture. After 10 minutes, 100 uL of HCl aqueous solution (1 M) was added to the solution, and the color of the solution turned tangerine. The reaction was lasted for 8 hours. The crude products were collected by centrifugation and then washed three times with CH_2Cl_2. The precipitate was then dissolved in DMF and diffused by CH_3CH_2OH at room temperature. After a week, red crystals were obtained. The yield was ~25% based on the Ag element (calculated from the $AgNO_3$) for synthesizing the $Ag_{29}(BDTA)_{12}(PPh_3)_4$ nanocluster.

Synthesis of the $Ag_{32}(BDTA)_{12}(PPh_3)_{10}$ nanocluster (Ag_{32} for short)

The synthesis of the Ag_{32} nanocluster was similar to Ag_{29}, except that 10 uL of the HCl aqueous solution (1 M) was added to the solution during the synthesis. The yield was ~20% based on the Ag element (calculated from the $AgNO_3$) for synthesizing the $Ag_{32}(BDTA)_{12}(PPh_3)_{10}$ nanocluster.

Synthesis of the $Ag_{33}(BDTA)_{12}(PPh_3)_{11}$ nanocluster (Ag_{33} for short)

The synthesis of the Ag_{33} nanocluster was similar to Ag_{29}, except that no HCl aqueous solution was added during the synthesis. The yield was ~10% based on the Ag element (calculated from the $AgNO_3$) for synthesizing the $Ag_{33}(BDTA)_{12}(PPh_3)_{11}$ nanocluster.

Transformation from Ag_{32}/Ag_{33} to Ag_{29} in the acidic environment

5 mg of the Ag_{32} or Ag_{33} nanocluster was dissolved in 20 mL of DMF, to which solution 5 uL of the HCl aqueous solution (1 M) was added. After 20 minutes, the cluster products were precipitated by adding 100 mL of CH_2Cl_2 to the solution. The ESI-MS measurement was performed to indicate the generation of Ag_{29} and the successful transformation from Ag_{32} or Ag_{33} to Ag_{29}. Of note, the Ag_{32} or Ag_{33} nanocluster was highly stable without the HCl aqueous solution and remained

unchanged for more than seven days.

Characterizations

The optical absorption spectra of nanoclusters were recorded using an Agilent 8453 diode array spectrometer.

The photoluminescence spectra of nanoclusters were measured on an FL-4500 spectrofluorometer with the same optical density.

Quantum yields (QYs) were measured with dilute solutions of nanoclusters on a HORIBA FluoroMax-4P.

ESI-MS measurements were performed by Waters XEVO G2-XS QT of the mass spectrometer. The sample was directly infused into the chamber at 5 μl/min. For preparing the ESI samples, nanoclusters were dissolved in DMF (1 mg/ml) and diluted (v/v = 1:1) by CH_3OH.

Element analysis (EA) was performed on Vario EL cube. 5 mg of each cluster sample was used in the experiment.

^{31}P nuclear magnetic resonance (NMR) spectra were acquired using a Bruker 600 AVANAC III spectrometer equipped with a Bruker BBO multinuclear probe (BrukerBioSpin, Rheinstetten, Germany). To achieve a sufficient signal-to-noise ratio, the ^{31}P NMR spectra were recorded by collecting 1k scans with a recycle delay time of 5s.

The CD spectra were measured on a JASCO J-1500 CD spectrophotometer. The solid samples were measured with a DRCD-574 solid samples accessories, using an integrating sphere to detect the diffuse reflectance of samples. For CD measurements, the parameters were set as follows: the scanning speed of 100 nm/min, the response time of 1 s, the bandwidth of 1 nm, the slit width of 3000 μm, the measure range of 250-900 nm, and the accumulation of 3.

The CPL spectra of nanoclusters were recorded using a JASCO CPL-300 instrument. For CPL measurements, the parameters were set as follows: the excitation wavelength of 450 nm, the excitation bandwidth of 10 nm, the emission slit width of 3000 μm, the scanning speed of 200 nm/min, the response time of 2 s, the measure range of 600-1000 nm, and the accumulation of 6.

The CPL sample preparation procedure was as follows:

(i) For bulk crystals: selected a bulk crystal and glued it to a quartz plate using silicone oil, and the CPL measurements of the crystal on different faces was achieved by flipping the quartz plate to adjust the angle of light incidence.

(ii) For microcrystalline samples: the bulk crystal was crushed into multiple microcrystals, and then glued them to the quartz plate using silicone oil. The other testing methods remained the same as those for bulk crystals.

Density functional theory (DFT) calculations

In this work, structural optimizations, transition-state searches, and energy barrier calculations of silver clusters were performed using Perdew-Burke-Ernzerhof (PBE)[3] exchange-correlation functional implemented in DMol[3] program.[4,5] The DFT-based relativistic semicore pseudopotential (DSPP), double-numerical plus d-polarization function (DND) basis sets, and the Tkatchenko-Scheffler (TS) dispersion correction were adopted in geometry optimization calculations and the search of transition state structures.[6-8] The convergence threshold for self-consistent-field (SCF) iteration was set to 1.0×10^{-5} Hartree. A Fermi smearing parameter of 0.002 Hartree was used in the DFT calculations. The convergence criteria of the geometric optimization were set to 1.0×10^{-5}

Hartree for the energy change, 2.0×10^{-3} Hartree/Å for the gradient, and 5.0×10^{-3} Å for the displacement. Transition states (TSs) search was computed using a combination of the liner and quadratic synchronous transit (LST/QST) methods. For all silver clusters, the BDTA and PPh_3 ligands were adopted in the DFT calculations.

The analysis of orbit weight double descriptors was completed by Gaussian 90 and Multiwfn 3.7 softwares.[9,10] The single-point calculations for silver clusters were carried out at PBE functional using Gaussian software. The structures of silver clusters adopted the geometric structure optimized by the DMol^3 software. The LANL2D2 basis set for Ag and 6-31g* basis set for C, H, P, O, S atoms were used in calculations.[11,12] Fukui function is an important concept in conceptual density functional theory, it has been widely used in prediction of reactive site. Therefore, condensed Fukui functions of nucleophilic (f^+), electrophilic (f^-), radical attack (f^0) and condensed dual descriptors (CDD) of silver clusters were calculated with Multiwfn 3.7.

Specifically, Fukui function is defined as:

$$f(r) = \left[\frac{\partial \rho(r)}{\partial N}\right]_v$$

where *ρ(r)* is the electron density at a point **r** in space, N is the number of electrons and the constant term *v* in the partial derivative is the external potential.

The f^+, f^-, f^0 and CDD can be calculated by:

Nucleophilic attack: $f^+(r) = \rho_{N+1}(r) - \rho_N(r)$

Electrophilic attack: $f^-(r) = \rho_N(r) - \rho_{N-1}(r)$

Radical attack: $f^0(r) = \frac{f^+(r) + f^-(r)}{2} = \frac{\rho_{N+1}(r) - \rho_{N-1}(r)}{2}$

Condensed dual descriptor (CDD): $\Delta f(r) = f^+(r) - f^-(r)$

If Δf > 0, then the site is favorable for a nucleophilic attack, whereas if Δf < 0, then the site is favorable for an electrophilic attack.

X-Ray Crystallography

The data collection for single-crystal X-ray diffraction (SC-XRD) of all nanocluster crystal samples was carried out on a Stoe Stadivari diffractometer under nitrogen flow, using graphite-monochromatized Cu Kα radiation (λ = 1.54186 Å). Data reductions and absorption corrections were performed using the SAINT and SADABS programs, respectively. The structure was solved by direct methods and refined with full-matrix least squares on F^2 using the SHELXTL software package. All non-hydrogen atoms were refined anisotropically, and all the hydrogen atoms were set in geometrically calculated positions and refined isotropically using a riding model. All crystal structures were treated with PLATON SQUEEZE. The diffuse electron densities from these residual solvent molecules were removed. The CCDC number of the $Ag_{29}(BDTA)_{12}(PPh_3)_4$ nanocluster is 2243513. The CCDC number of the $Ag_{32}(BDTA)_{12}(PPh_3)_{10}$ nanocluster is 2243517. The CCDC number of the chiral $Ag_{33}(BDTA)_{12}(PPh_3)_{11}$ (*S* enantiomer) nanocluster is 2243519. The CCDC number of the chiral $Ag_{33}(BDTA)_{12}(PPh_3)_{11}$ (*R* enantiomer) nanocluster is 2243542.

Scheme S1. The procedures for selecting Ag_{33} nanocluster single crystals towards SC-XRD and CD/CPL measurements.

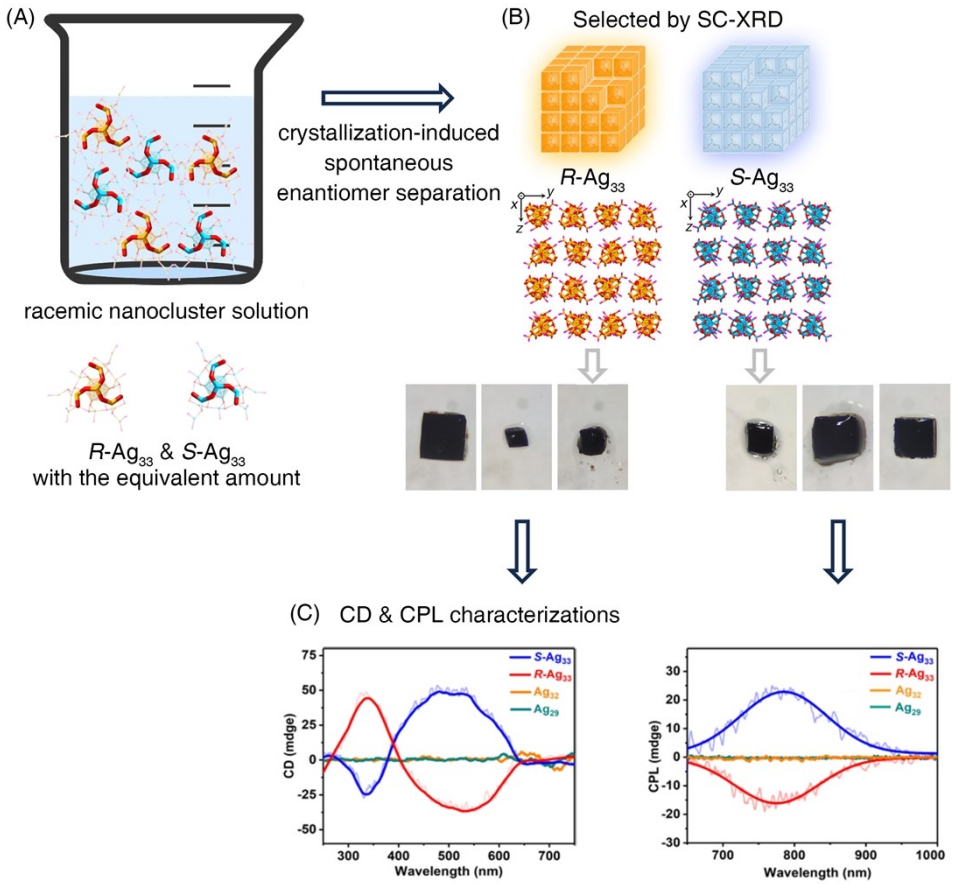

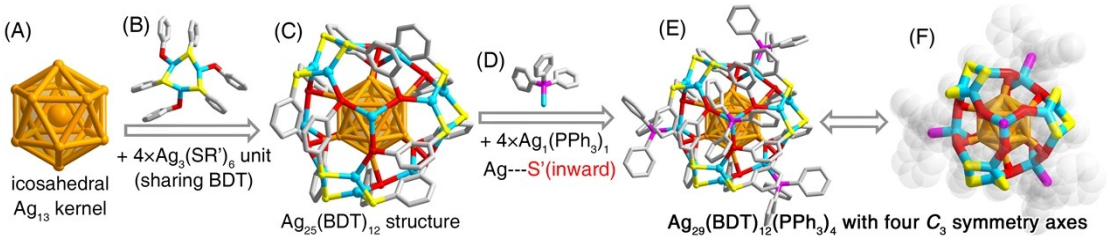

Fig. S1. Structural anatomy of the $Ag_{29}(BDT)_{12}(PPh_3)_4$ nanocluster. (A) The icosahedral Ag_{13} kernel. (B) The $Ag_{12}(BDT)_{12}$ surface structure contains four $Ag_3(SR')_6$ surface units via sharing the bidentate BDTA thiol ligands. (C) The $Ag_{25}(BDT)_{12}$ structure. (D) The four $Ag_1(PPh_3)_1$ vertex units. (E,F) The overall structure of the $Ag_{29}(BDT)_{12}(PPh_3)_4$ nanocluster with four C_3 symmetry axes. Color legends: orange/light blue spheres, Ag; red spheres, outward S; yellow spheres, inward S; magenta spheres, P; grey spheres, C. All H atoms are omitted for clarity.

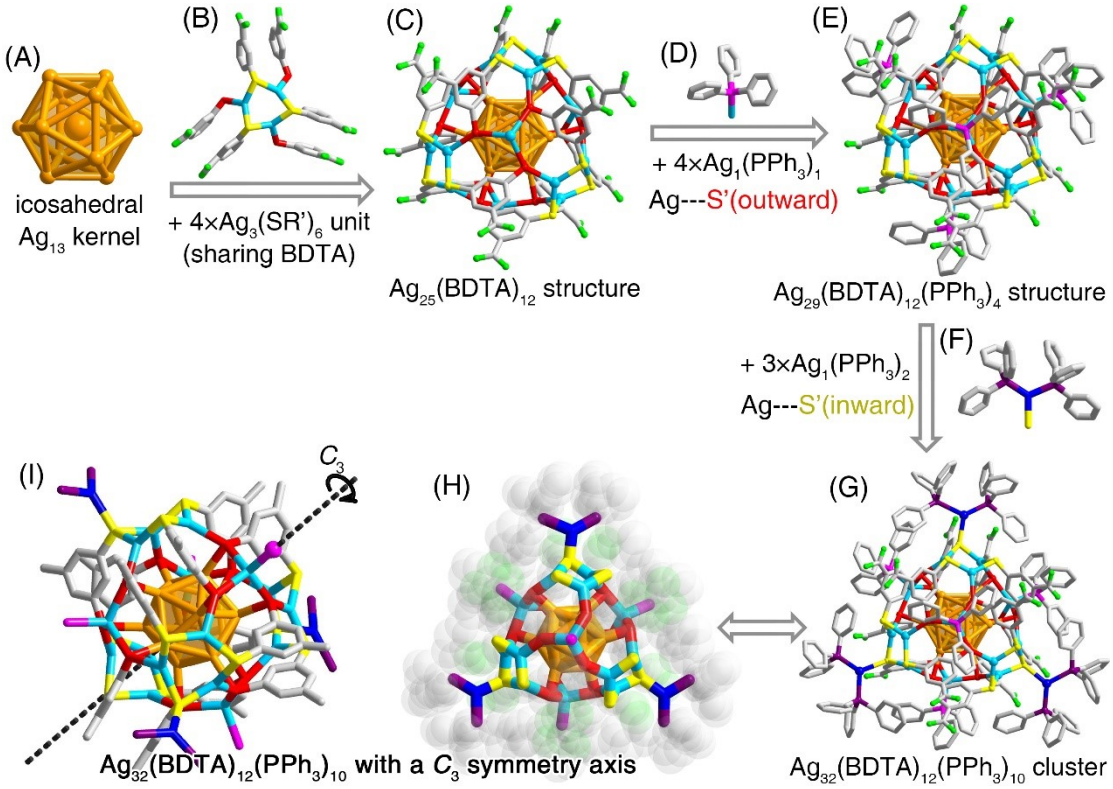

Fig. S2. Structural anatomy of the $Ag_{32}(BDTA)_{12}(PPh_3)_{10}$ nanocluster. (A) The icosahedral Ag_{13} kernel. (B) The $Ag_{12}(BDTA)_{12}$ surface structure contains four $Ag_3(SR')_6$ surface units via sharing the bidentate BDTA thiol ligands. (C) The $Ag_{25}(BDTA)_{12}$ structure. (D) The four $Ag_1(PPh_3)_1$ vertex units. (E) The $Ag_{29}(BDTA)_{12}(PPh_3)_4$ structure. (F) The three $Ag_1(PPh_3)_2$ surface symmetrical expanding units. (G,H) The overall structure of the $Ag_{32}(BDTA)_{12}(PPh_3)_{10}$ nanocluster. (I) The overall configuration of the $Ag_{32}(BDTA)_{12}(PPh_3)_{10}$ nanocluster contains a C_3 symmetry axis, passing through a vertex PPh_3 ligand and the innermost Ag core. Color legends: orange/light blue/blue spheres, Ag; red/yellow spheres, S; magenta/purple spheres, P; green sphere, O; grey sphere, C. All H atoms are omitted for clarity.

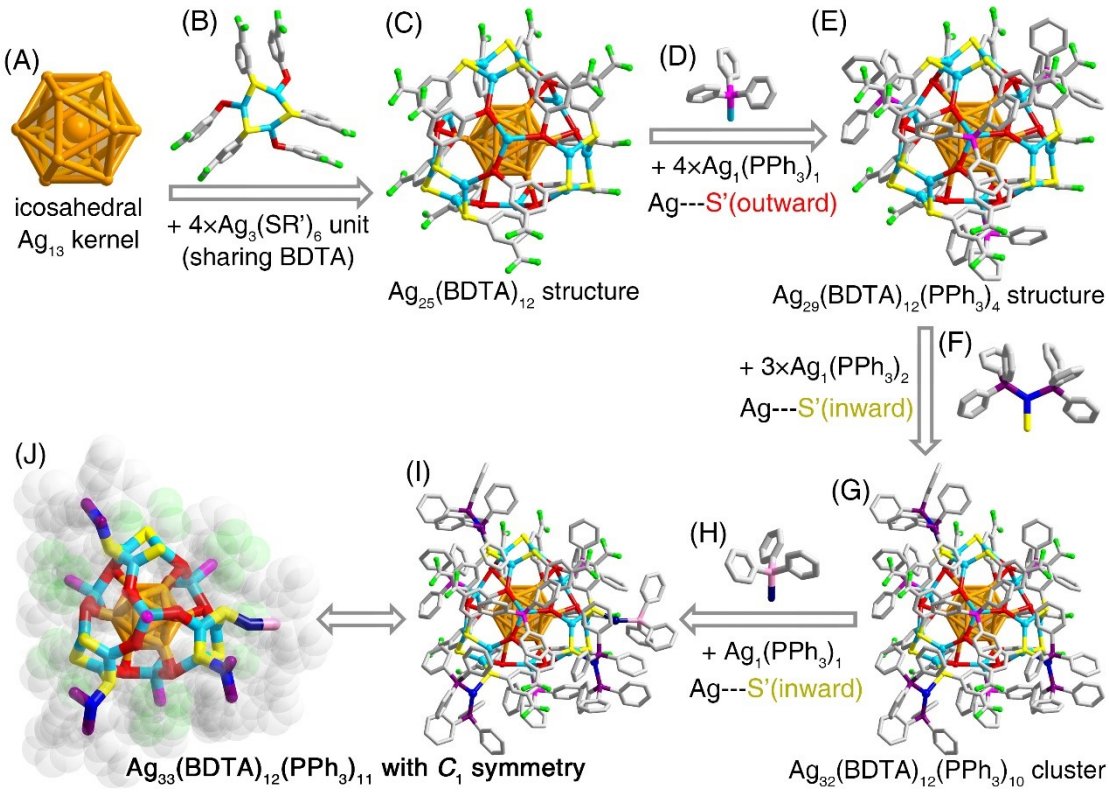

Fig. S3. Structural anatomy of the $Ag_{33}(BDTA)_{12}(PPh_3)_{11}$ nanocluster. (A) The icosahedral Ag_{13} kernel. (B) The $Ag_{12}(BDTA)_{12}$ surface structure contains four $Ag_3(SR')_6$ surface units via sharing the bidentate BDTA thiol ligands. (C) The $Ag_{25}(BDTA)_{12}$ structure. (D) The four $Ag_1(PPh_3)_1$ vertex units. (E) The $Ag_{29}(BDTA)_{12}(PPh_3)_4$ structure. (F) The three $Ag_1(PPh_3)_2$ surface symmetrical expanding units. (G) The $Ag_{32}(BDTA)_{12}(PPh_3)_{10}$ structure. (H) The $Ag_1(PPh_3)_1$ surface asymmetrical expanding unit. (I,J) The overall structure of the $Ag_{33}(BDTA)_{12}(PPh_3)_{11}$ nanocluster. Color legends: orange/light blue/blue spheres, Ag; red/yellow spheres, S; magenta/purple/pink spheres, P; green sphere, O; grey sphere, C. All H atoms are omitted for clarity.

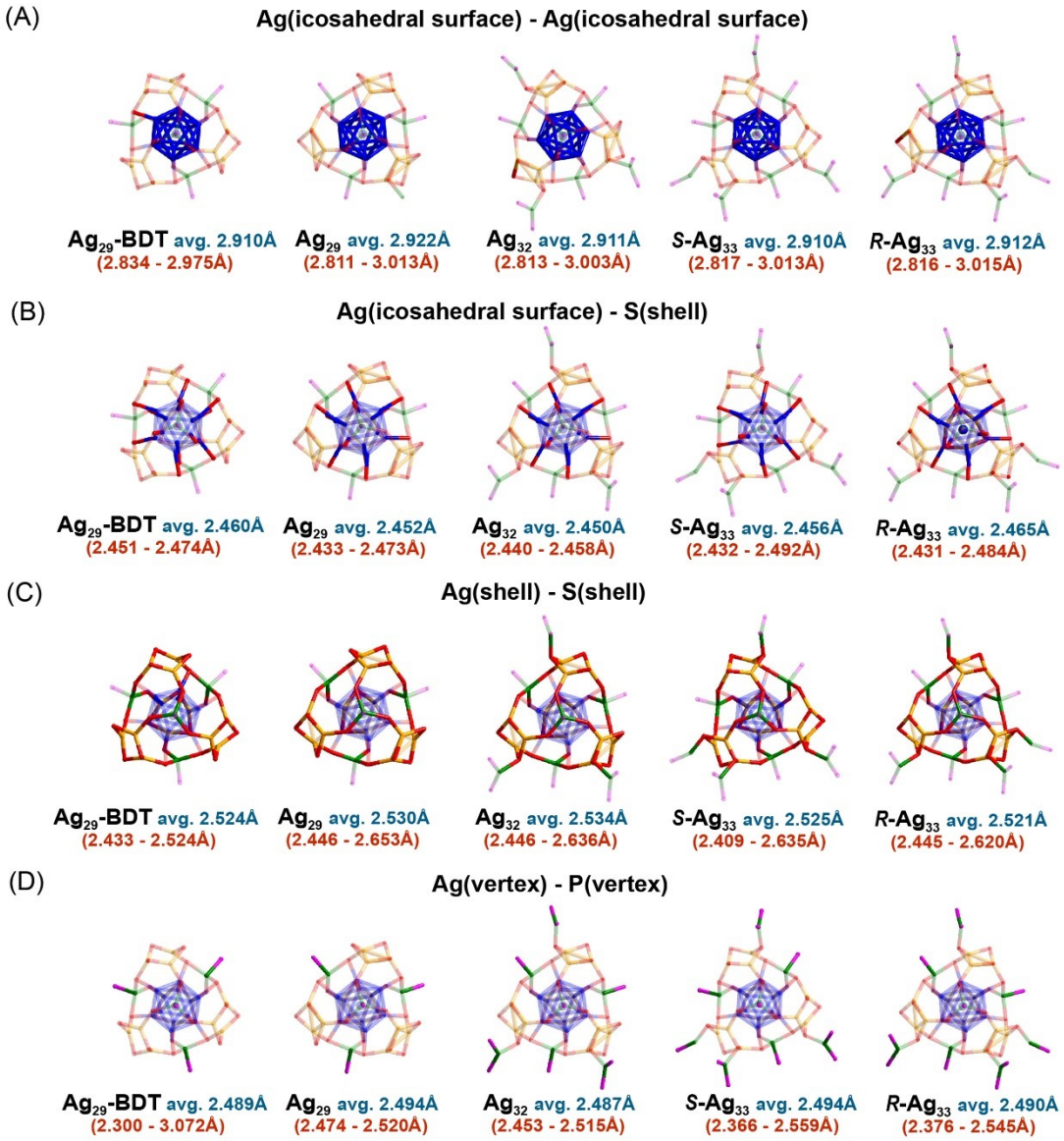

Fig. S4. Comparison of the corresponding bond lengths among different nanoclusters. (A) Comparison of the length of the Ag(icosahedral surface)---Ag(icosahedral surface) bonds in Ag_{29}-BDT, Ag_{29}, Ag_{32}, *S*-Ag_{33}, and *R*-Ag_{33} nanoclusters. (B) Comparison of the length of the Ag(icosahedral surface)---S(shell) bonds in Ag_{29}-BDT, Ag_{29}, Ag_{32}, *S*-Ag_{33}, and *R*-Ag_{33} nanoclusters. (C) Comparison of the length of the Ag(shell)---S(shell) bonds in Ag_{29}-BDT, Ag_{29}, Ag_{32}, *S*-Ag_{33}, and *R*-Ag_{33} nanoclusters. (D) Comparison of the length of the Ag(vertex)---P(vertex) bonds in Ag_{29}-BDT, Ag_{29}, Ag_{32}, *S*-Ag_{33}, and *R*-Ag_{33} nanoclusters.

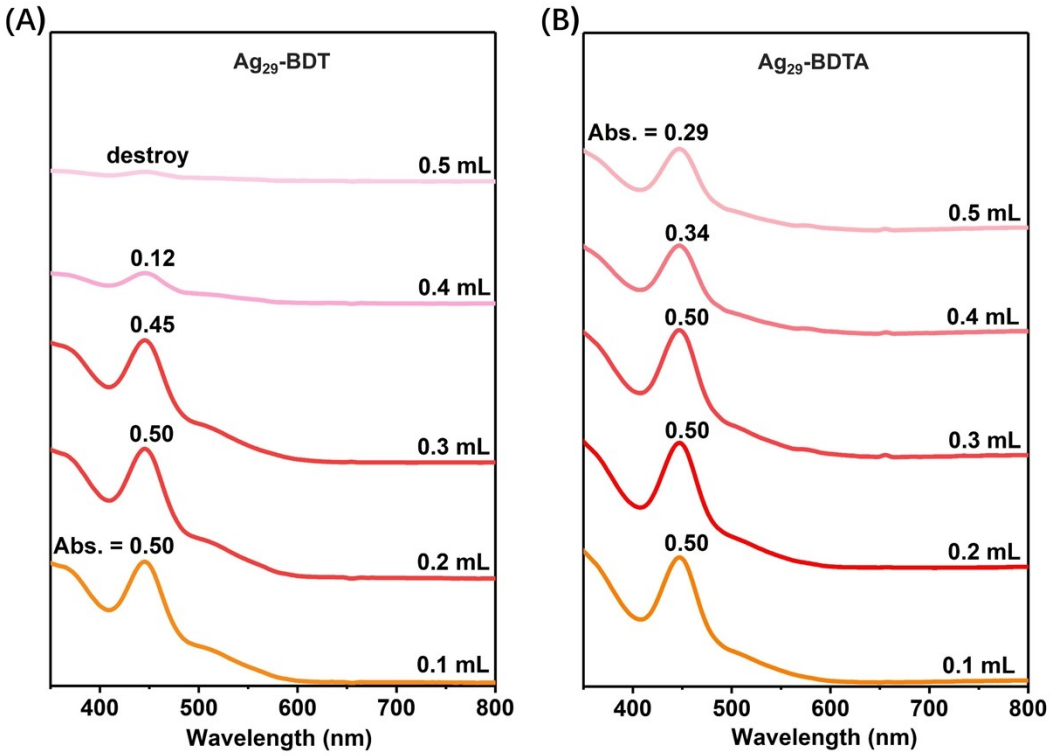

Fig. S5. Stability comparison between Ag_{29} and Ag_{29}-BDT nanoclusters in acidic environment. UV-vis absorptions of (A) Ag_{29}-BDT and (B) Ag_{29}-BDTA with different introduction of HCl aqueous (0.1 M).

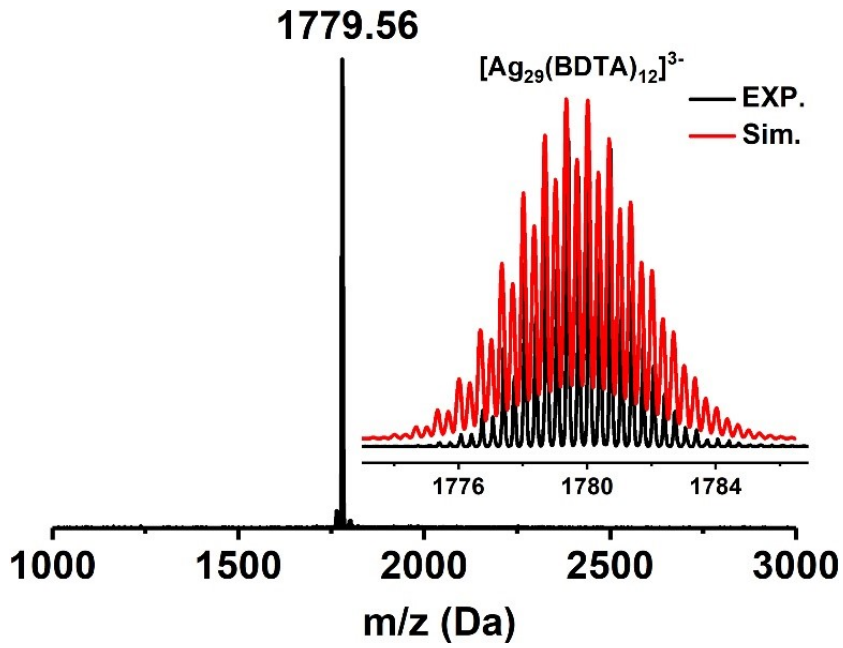

Fig. S6. ESI-MS result of the $Ag_{29}(BDTA)_{12}(PPh_3)_4$ nanocluster in the negative mode. The magnification of the peak suggested a "–3" charge state of the nanocluster, i.e., $[Ag_{29}(BDTA)_{12}]^{3-}$, since this peak evidenced a characteristic isotopic pattern with peaks separated by a m/z of 0.33 Da. No "cluster + PPh_3" signal was observed in the mass result.

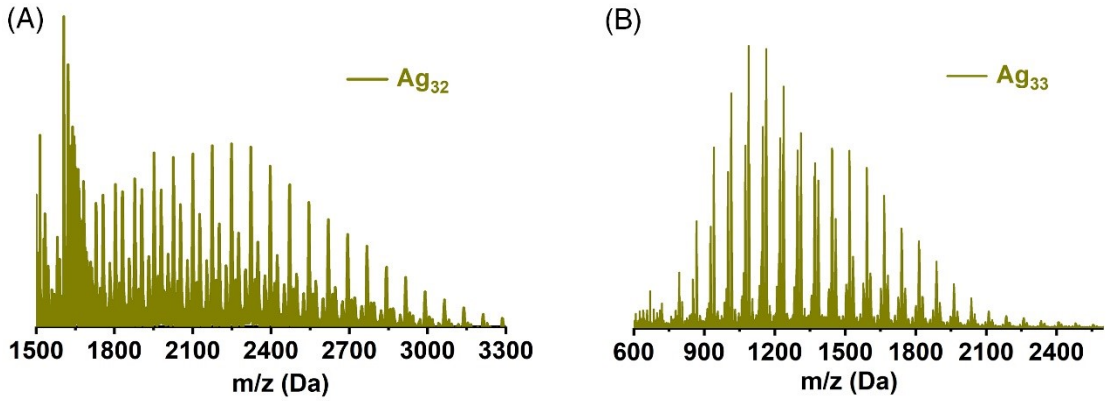

Fig. S7. (A) ESI-MS result of the $Ag_{32}(BDTA)_{12}(PPh_3)_{10}$ nanocluster in the mass range from 1500 to 3300 Da. (B) ESI-MS result of the $Ag_{33}(BDTA)_{12}(PPh_3)_{11}$ nanocluster in the mass range from 600 to 2600 Da.

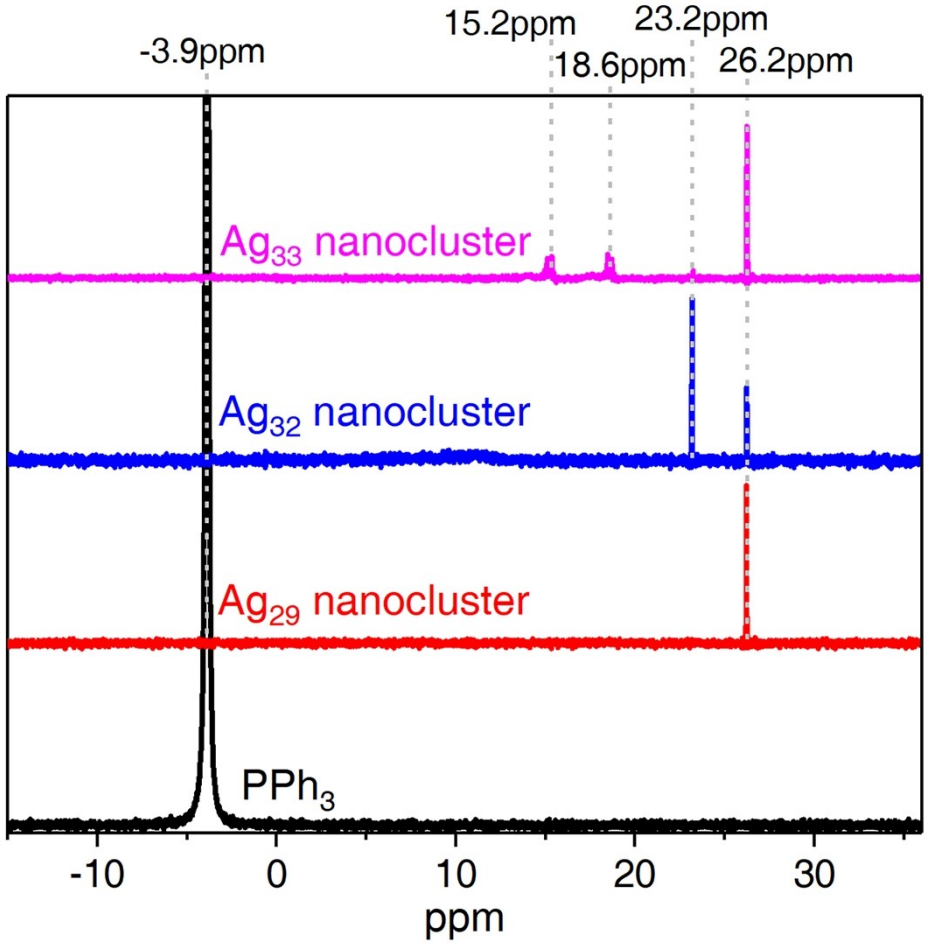

Fig. S8. ^{31}P NMR results of the obtained silver nanoclusters. The ^{31}P NMR signal of PPh_3 (black line) located at -3.9 ppm, which was absent for each cluster sample. The ^{31}P NMR result of the $Ag_{29}(BDTA)_{12}(PPh_3)_4$ nanocluster (red line) showed only one signal at 26.2 ppm, demonstrating that all phosphine ligands followed the same coordination environment in the cluster framework, matching well with the crystal structure of $Ag_{29}(BDTA)_{12}(PPh_3)_4$. The ^{31}P NMR result of the $Ag_{32}(BDTA)_{12}(PPh_3)_{10}$ nanocluster (blue line) exhibited two signals, locating at 26.2 and 23.2 ppm, respectively. The 26.2 ppm signal originated from the four vertex PPh_3 ligands (highlighted in

magenta in Figure 1), the same as those in $Ag_{29}(BDTA)_{12}(PPh_3)_4$, and the 23.2 ppm came from the six PPh_3 ligands of the three $Ag_1(PPh_3)_2$ surface symmetrical expanding units (highlighted in purple in Figure 1). In this context, the integral area of the 23.2 ppm signal was much larger than that at 26.2 ppm. The ^{31}P NMR result of the $Ag_{33}(BDTA)_{12}(PPh_3)_{11}$ nanocluster (magenta line) exhibited several signals at 26.2, 23.2, 18.6, and 15,2 ppm, which was rational by considering that the PPh_3 ligands in the $Ag_{33}(BDTA)_{12}(PPh_3)_{11}$ nanocluster followed several different coordination environments, including the vertex PPh_3 ligand, the $Ag_1(PPh_3)_2$ surface symmetrical expanding unit, and the $Ag_1(PPh_3)_1$ surface asymmetrical expanding unit. Indeed, the integral area of the 23.2, 18.6, and 15,2 ppm signal was much larger than that at 26.2 ppm. In this context, the ^{31}P NMR results confirmed the symmetrical arrangement of the Ag_{29} and Ag_{32} cluster frameworks as well as the asymmetrical arrangement of the Ag_{33} cluster framework.

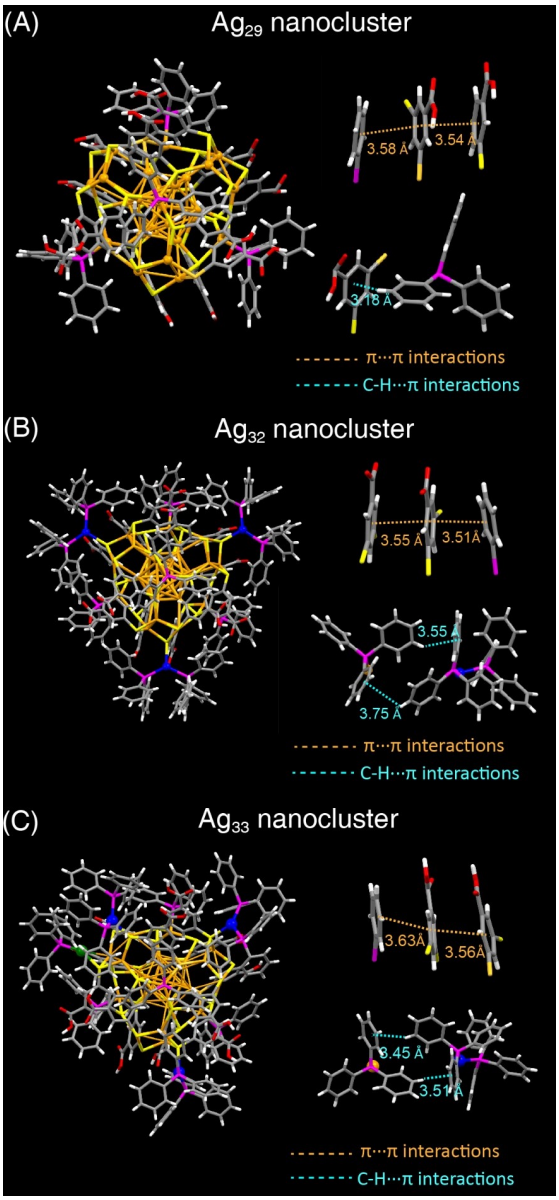

Fig. S9. Intracluster C-H···π and π···π···π interactions of (A) Ag_{29}, (B) Ag_{32}, and (C) Ag_{33} nanoclusters.

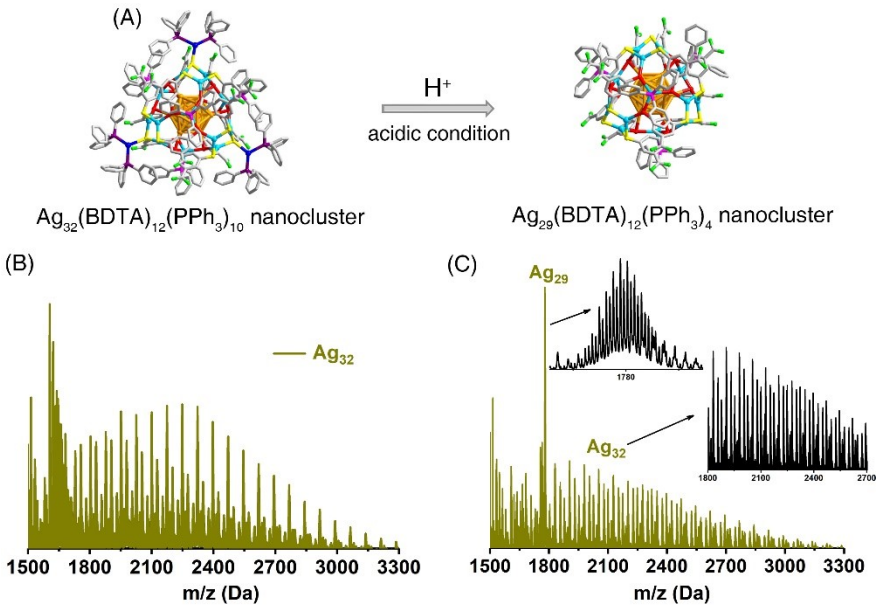

Fig. S10. (A) Schematic illustration of the transformation from $Ag_{32}(BDTA)_{12}(PPh_3)_{10}$ to $Ag_{29}(BDTA)_{12}(PPh_3)_4$ induced by the acidic condition. (B) ESI-MS result of the $Ag_{32}(BDTA)_{12}(PPh_3)_{10}$ nanocluster before the H^+ addition. (C) ESI-MS result of the $Ag_{32}(BDTA)_{12}(PPh_3)_{10}$ nanocluster after the H^+ addition. A mass signal of the $[Ag_{29}(BDTA)_{12}]^{3-}$ nanocluster was observed, demonstrating the transformation from $Ag_{32}(BDTA)_{12}(PPh_3)_{10}$ to $Ag_{29}(BDTA)_{12}(PPh_3)_4$.

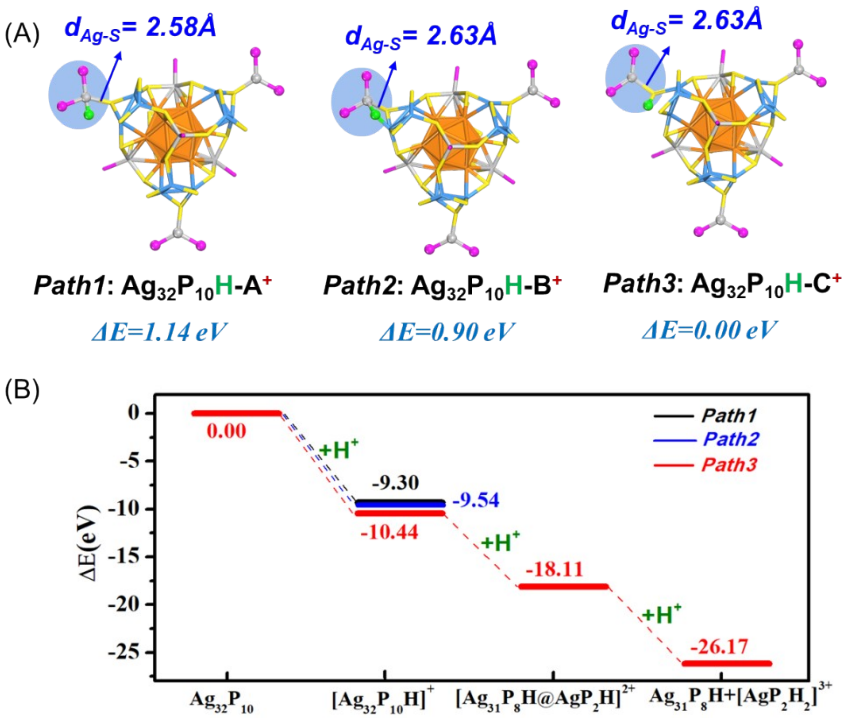

Fig. S11. (A) Structures and relative energies of three $Ag_{32}P_{10}H^+$ isomers. (B) Reaction pathways and energy curves of the degradation of the Ag_{32} nanocluster to form the Ag_{31} nanocluster in an acidic environment. Color legends: orange/light blue/grey, Ag; yellow, S; magenta, P; green, H. All R groups are omitted for clarity.

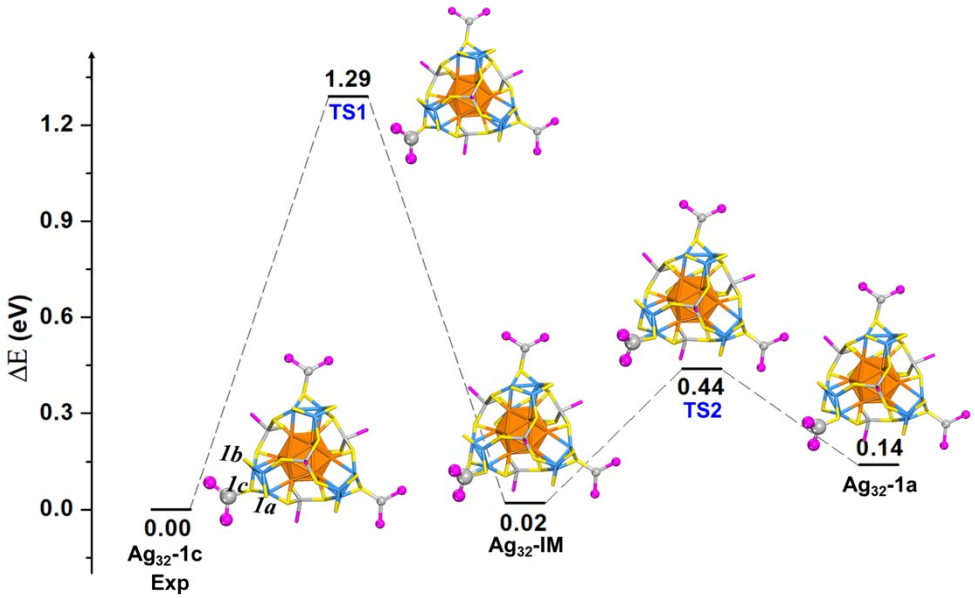

Fig. S12. The intermediate structures and the related energy curve of the Ag_{32} cluster during the migration of the $Ag(PPh_3)_2$ group from site 1c to 1a. Color legends: orange/light blue/grey, Ag; yellow, S; magenta, P. All R groups are omitted for clarity.

Ag_{32}-Iso		Δf
1	S(*a*)	0.0021
	S(*b*)	-0.0011
	S(*c*)	-0.0062
2	S(*a*)	0.0006
	S(*b*)	0.0010
	S(*c*)	0.0079
3	S(*a*)	0.0008
	S(*b*)	0.0046
	S(*c*)	-0.0228

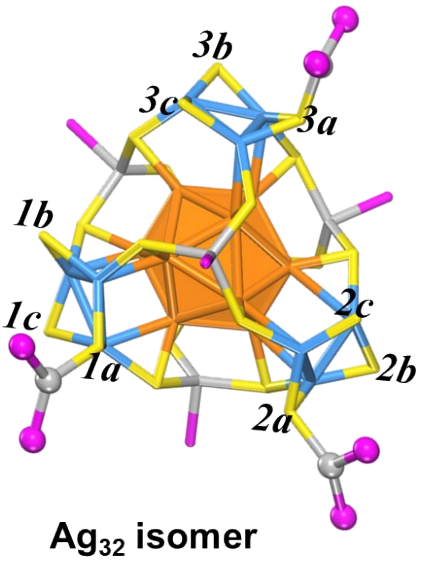

Fig. S13. The orbital-weighted dual descriptor of the S atoms on the Ag_{32} cluster isomer. Color legends: orange/light blue/grey, Ag; yellow, S; magenta, P. All R groups are omitted for clarity.

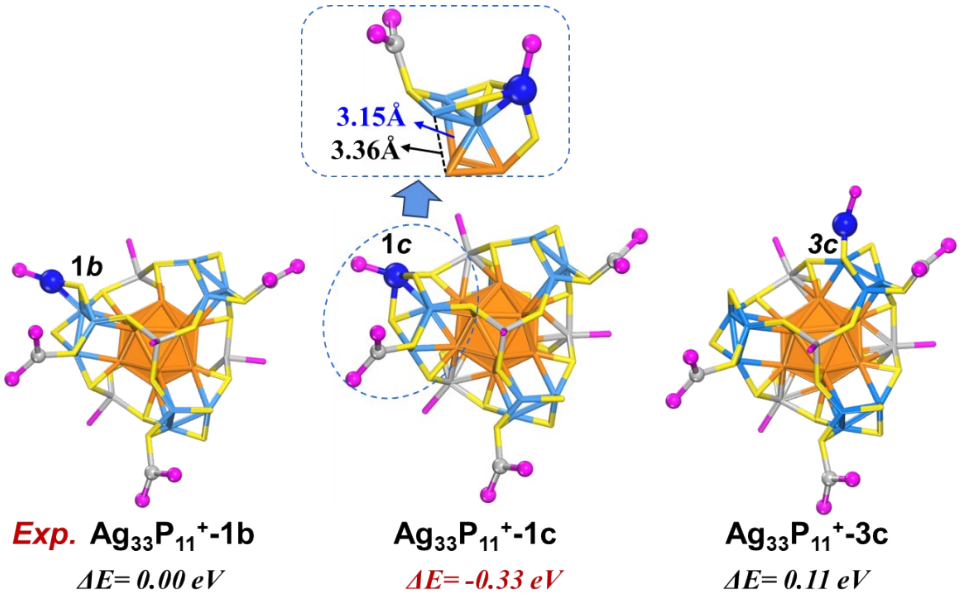

Fig. S14. Structures and relative energies of three $Ag_{33}P_{11}^{+}$ cluster isomers. Color legends: orange/light blue/blue/grey, Ag; yellow, S; magenta, P. All R groups are omitted for clarity.

(A)

	Ag_{29}	Ag_{32}	*S*-Ag_{33}	*R*-Ag_{33}
Crystal system	monoclinic	trigonal	orthorhombic	orthorhombic
Space group	P 21/n	R -3 c	P 21 21 21	P 21 21 21
a, b, c/Å	28.6819(11) 25.1945(9) 33.0107(12)	26.3342(13) 26.3342(13) 197.728(11)	29.637(2) 32.888(3) 34.685(4)	29.5928(17) 32.9084(18) 34.479(5)
α, β, γ/Å	90 90.937 90	90 90 120	90 90 90	90 90 90
Volume/Å^3	23851.2(15)	118751(13)	33808(5)	33578(6)
Z	4	12	4	4

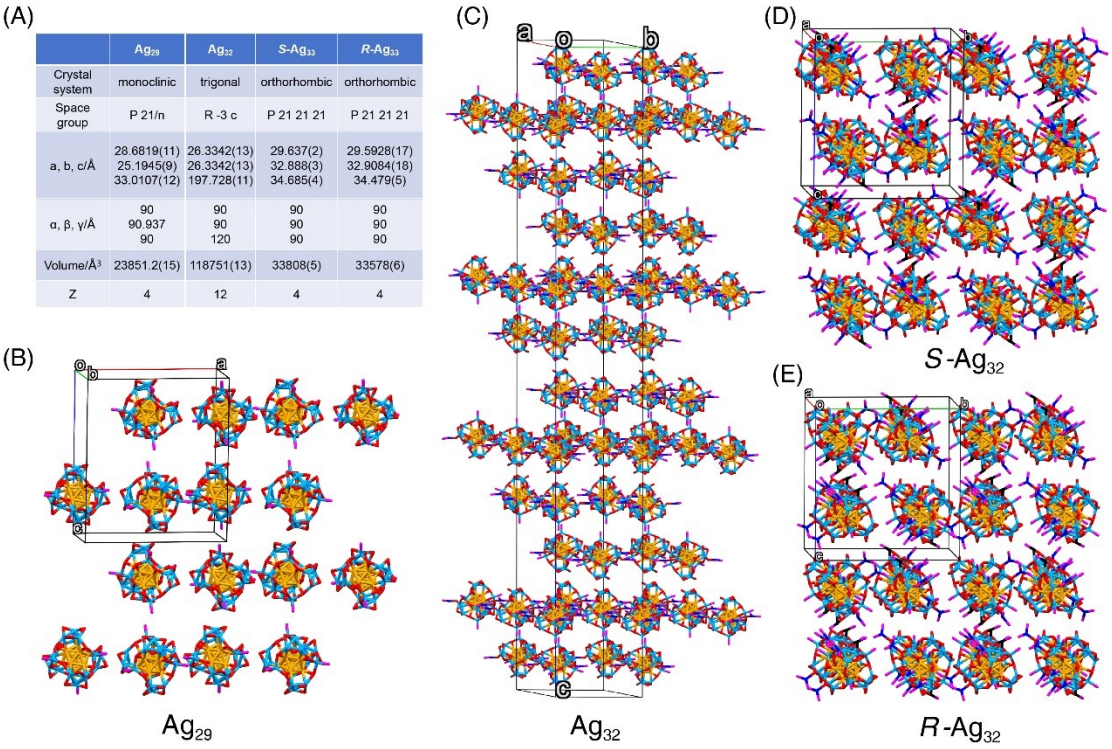

Fig. S15. (A) Comparison of the crystalline unit cell parameters of these structure-correlated silver nanoclusters.Crystal lattices of (B) Ag_{29}, (C) Ag_{32}, (D) *S*-Ag_{33}, and (E) *R*-Ag_{33} nanoclusters.

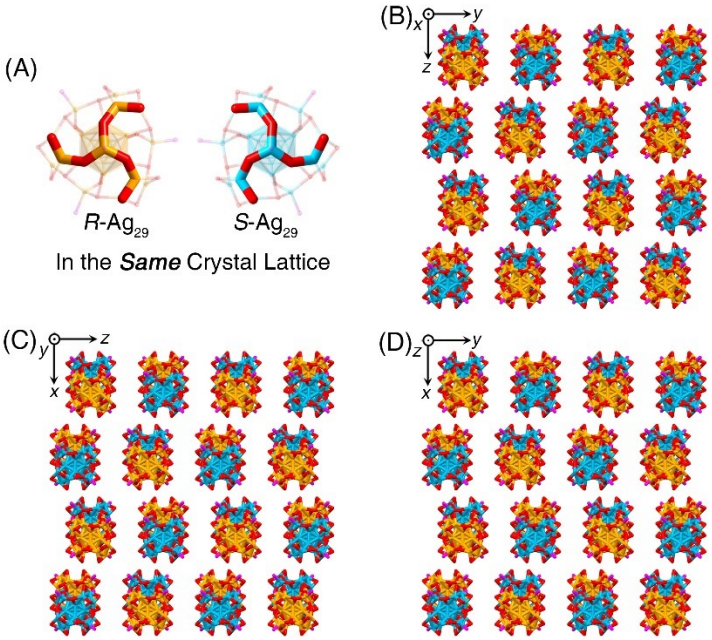

Fig. S16. (A) Structures of *R*-Ag_{29} and *S*-Ag_{29} enantiomers in the same crystal lattice. (B-D) Packing of Ag_{29} nanoclusters in the crystal lattice: view from the *x* axis (B), *y* axis (C), and *z* axis (D).

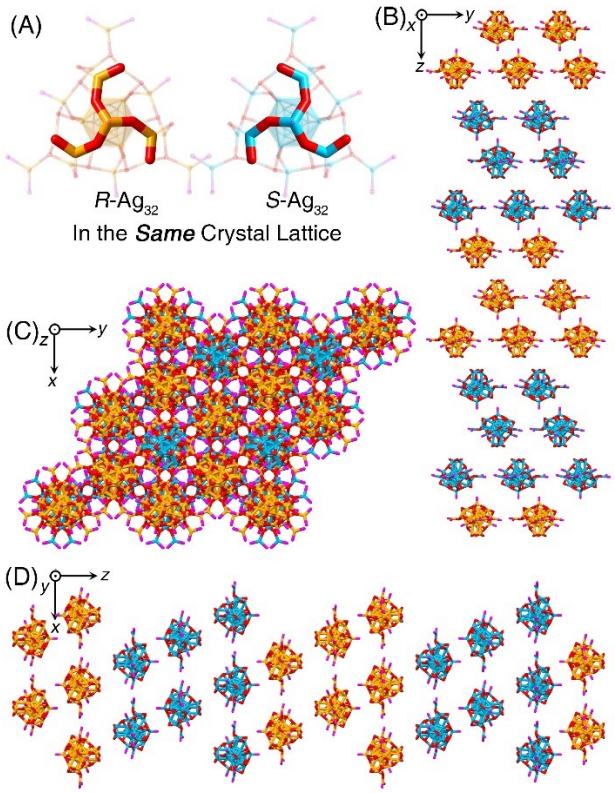

Fig. S17. (A) Structures of *R*-Ag_{32} and *S*-Ag_{32} enantiomers in the same crystal lattice. (B-D) Packing of Ag_{32} nanoclusters in the crystal lattice: view from the *x* axis (B), *z* axis (C), and *y* axis (D).

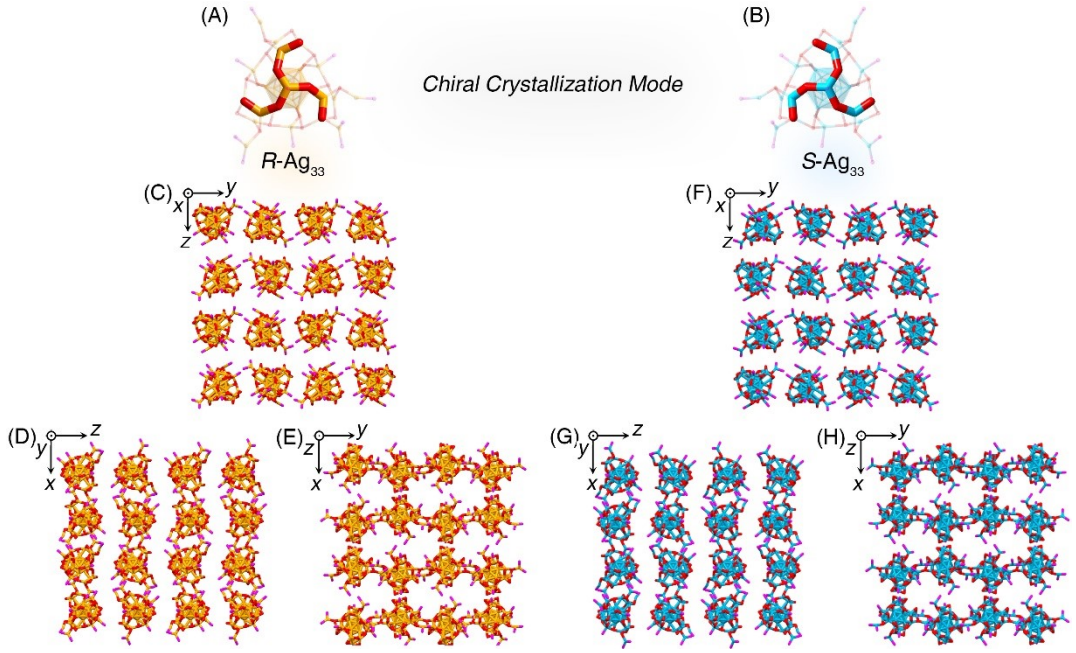

Fig. S18. (A) Structure of the *R*-Ag_{33} nanocluster enantiomer. (B) Structure of the *S*-Ag_{33} nanocluster enantiomer. (C-E) Packing of *R*-Ag_{33} nanoclusters in the crystal lattice: view from the *x* axis (C), *y* axis (D), and *z* axis (E). (F-H) Packing of *S*-Ag_{33} nanoclusters in the crystal lattice: view from the *x* axis (F), *y* axis (G), and *z* axis (H).

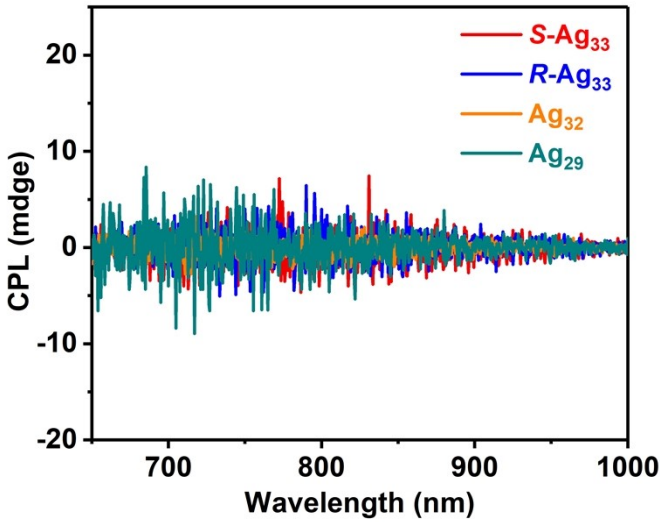

Fig. S19. CPL spectra of cluster samples in the solution state.

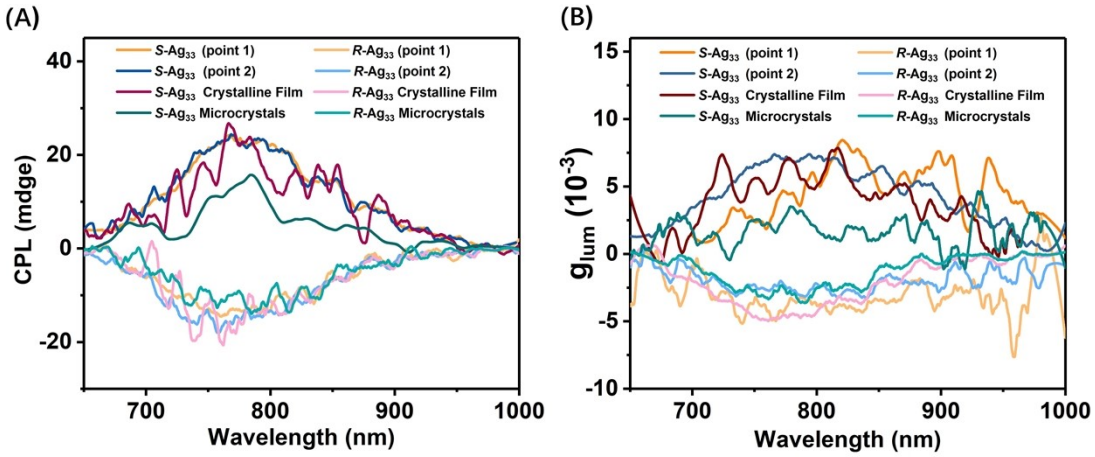

Fig. S20. Verification of the optical activity of Ag_{33} crystal in different test state. (a) CPL spectra and (b) corresponding glum spectra of Ag_{33} crystals at different test point (point 1 and point 2 were selected from the front and back sides of the crystal, respectively) and microcrystals (obtained by crushing the Ag_{33} crystals).

Table S1. Crystal data and structure refinement for the $Ag_{29}(BDTA)_{12}(PPh_3)_4$ nanocluster.

Crystal system	monoclinic
Space group	P 21/n
a/Å	28.6819(11)
b/Å	25.1945(9)
c/Å	33.0107(12)
α/°	90
β/°	90.937(3)
γ/°	90
Volume/Å^3	23851.2(15)
Z	4
ρcalcg/cm^3	1.779
μ/mm^{-1}	21.199
F(000)	12124
Crystal size/mm^3	0.1×0.1×0.1
Radiation	CuKa (λ = 1.54186)
Index ranges	-33 ≤ h ≤ 26, -22 ≤ k ≤ 29, -38 ≤ l ≤ 38
Final R indexes [I>=2σ (I)]	R_1 = 0.0922, wR_2 = 0.2454
Final R indexes [all data]	R_1 = 0.1220, wR_2 = 0.2832

Table S2. Crystal data and structure refinement for the $Ag_{32}(BDTA)_{12}(PPh_3)_{10}$ nanocluster.

Crystal system	trigonal
Space group	R -3 c
a/Å	26.3342(11)
b/Å	26.3342(11)
c/Å	197.728(12)
α/°	90
β/°	90
γ/°	120
Volume/Å^3	118754
Z	12
ρcalcg/cm^3	1.390
μ/mm^{-1}	14.265
F(000)	45381
Crystal size/mm^3	0.1×0.1×0.1
Radiation	CuKa (λ = 1.54186)
Index ranges	-30 ≤ h ≤ 16, -29 ≤ k ≤ 26, -184 ≤ l ≤ 227
Final R indexes [I>=2σ (I)]	R_1 = 0.0939, wR_2 = 0.2790
Final R indexes [all data]	R_1 = 0.1366, wR_2 = 0.3338

Table S3. Crystal data and structure refinement for the *S*-$Ag_{33}(BDTA)_{12}(PPh_3)_{11}$ nanocluster.

Crystal system	orthorhombic
Space group	P 21 21 21
a/Å	29.637(2)
b/Å	32.888(3)
c/Å	34.685(4)
α/°	90
β/°	90
γ/°	90
Volume/$Å^3$	33808(5)
Z	4
ρcalcg/cm^3	1.3659
μ/mm^{-1}	17.180
F(000)	16187
Crystal size/mm^3	0.1×0.1×0.1
Radiation	CuKa (λ = 1.54186)
Index ranges	-33 ≤ h ≤ 15, -33 ≤ k ≤ 36, -30 ≤ l ≤ 38
Final R indexes [I>=2σ (I)]	R_1 = 0.0813, wR_2 = 0.1866
Final R indexes [all data]	R_1 = 0.1377, wR_2 = 0.2105

Table S4. Crystal data and structure refinement for the *R*-$Ag_{33}(BDTA)_{12}(PPh_3)_{11}$ nanocluster.

Crystal system	orthorhombic
Space group	P 21 21 21
a/Å	29.5928(17)
b/Å	32.9084(18)
c/Å	34.479(5)
α/°	90
β/°	90
γ/°	90
Volume/$Å^3$	33587
Z	4
ρcalcg/cm^3	1.709
μ/mm^{-1}	17.337
F(000)	16728
Crystal size/mm^3	0.1×0.1×0.1
Radiation	CuKa (λ = 1.54186)
Index ranges	-14 ≤ h ≤ 33, -37 ≤ k ≤ 37, -39 ≤ l ≤ 39
Final R indexes [I>=2σ (I)]	R_1 = 0.0703, wR_2 = 0.1771
Final R indexes [all data]	R_1 = 0.0995, wR_2 = 0.2000

Table S5. Elemental analysis (EA) results of the obtained silver nanoclusters. The matching between calculated and experimental results demonstrated the purity of the obtained silver nanocluster crystals.

Sample	Elemental Analysis	
	Cal.	Exp.
$Ag_{29}(BDT)_{12}(PPh_3)_4$	C: 29.51%; H: 1.86%	C: 29.58%; H: 1.88%
$Ag_{29}(BDTA)_{12}(PPh_3)_4$	C: 29.33%; H: 1.70%	C: 29.20%; H: 1.72%
$Ag_{32}(BDTA)_{12}(PPh_3)_{10}$	C: 38.27%; H: 2.41%	C: 38.52%; H: 2.45%
$Ag_{33}(BDTA)_{12}(PPh_3)_{11}$	C: 39.13%; H: 2.48%	C: 39.01%; H: 2.53%

References

1. P. T. Corbett, J. K. M. Sanders, and S. Otto, *Angew. Chem. Int. Ed.* 2008, **14**, 2153-2166.
2. L. G. AbdulHalim, M. S. Bootharaju, Q. Tang, S. Del Gobbo, R. G. AbdulHalim, M. Eddaoudi, D.-e. Jiang, O. M. Bakr, *J. Am. Chem. Soc.,* 2015, **137**, 11970-11975.
3. J. P. Perdew, K. Burke, M. Ernzerhof, *Phys. Rev. Lett.* **1996**, **77**, 3865.
4. B. Delley, *Chem. Phys.* 1990, **92**, 508-517.
5. B. Delley, *Chem. Phys.* 2000, **113**, 7756-7764.
6. B. Delley, *J. Phys. Chem. A* 2006, **110**, 13632-13639.
7. B. Delley, *Phys. Rev. B* 2002, **66**, 1551259.
8. A. Tkatchenko, M. Scheffler, *Phys. Rev. Lett.* 2009, **102**, 073005.
9. M. J. Frisch, G. W. Trucks, H. B. Schlegel, G. E. Scuseria, M. A. Robb, J. R. Cheeseman, G. Scalmani, V. Barone, B. Mennucci, G. A. Petersson, H. Nakatsuji, M. Caricato, X. Li, H. P. Hratchian, A. F. Izmaylov, J. Bloino, G. Zheng, J. L. Sonnenberg, M. Hada, M. Ehara, K. Toyota, R. Fukuda, J. Hasegawa, M. Ishida, T. Nakajima, Y. Honda, O. Kitao, H. Nakai, T. Vreven, J. A. Montgomery, J. E. Peralta, F. Ogliaro, M. Bearpark, J. J. Heyd, E. Brothers, K. N. Kudin, V. N. Staroverov, R. Kobayashi, J. Normand, K. Raghavachari, A. Rendell, J. C. Burant, S. S. Iyengar, J. Tomasi, M. Cossi, N. Rega, J. M. Millam, M. Klene, J. E. Knox, J. B. Cross, V. Bakken, C. Adamo, J. Jaramillo, R. Gomperts, R. E. Stratmann, O. Yazyev, A. J. Austin, R. Cammi, C. Pomelli, J. W. Ochterski, R. L. Martin, K. Morokuma, V. G. Zakrzewski, G. A. Voth, P. Salvador, J. J. Dannenberg, S. Dapprich, A. D. Daniels, Farkas, J. B. Foresman, J. V. Ortiz, J. Cioslowski, D. J. Fox, *Gaussian 09*, Revision A.1; Wallingford, CT, 2009.
10. T. Lu, F. Chen, *J. Comput. Chem.* 2012, **33**, 580.
11. P. J. Hay, W. R. Wadt, *J. Chem. Phys.* 1985, **82**, 299-310.
12. W. J. Hehre, R. Ditchfield, J. A. Pople, *J. Chem. Phys.* 1972, **56**, 2257-2261.